# PNAS

## www.pnas.org

# Supplementary Information for

## Phyllotactic patterning of gerbera flower heads

**T Zhang, M Cieslak, A Owens, F Wang, SK Broholm, TH Teeri, P Elomaa, and P Prusinkiewicz**

**Paula Elomaa. E-mail: paula.elomaa@helsinki.fi**
**Przemyslaw Prusinkiewicz. E-mail: pwp@ucalgary.ca**

**This PDF file includes:**

Supplementary text
Figs. S1 to S11
Legends for Movies S1 to S7
SI References

**Other supplementary materials for this manuscript include the following:**

Movies S1 to S7

## Supporting Information Text

This text describes the computational models in more detail. In the description of patterning, we use the term "primordium" to denote both the incipient primordia (initia) and primordia that are already outgrowing.

## Main symbols

| | |
|---|---|
| $(r, \phi)$ | polar coordinates (radius, angle) of a primordium center on the receptacle |
| $(\rho, \theta)$ | polar coordinates (radius, angle) within a primordium |
| $r_a$ | active ring radius (circular) |
| $r_e$ | radial coordinate of a point on an elliptic active ring |
| $r_i$ | radial coordinate of primordium $i$ |
| $r_j$ | radial coordinate of sampling point $j$ on the active ring |
| $s$ | arc-length coordinate on the generative curve, normalized to interval $[0, 1]$ |
| $\rho_i$ | radius of primordium $i$ |
| $k_p$ | rate of change of parameter $p$ |
| $\Delta x$ | increment of variable $x$ |
| $t$ | simulation time |
| $w$ | material point coordinate on the generative curve |
| $d$ | distance |
| $Th_l$ | threshold length of the active ring segment for inserting a new primordium in Model 1 |
| $Th_d$ | threshold distance to neighbors for inserting a new primordium in Models 2 and 3 |
| $\lambda$ | controls asymmetry of primordium insertion in Model 1 |
| $B_m$ | B-spline of degree $m$ |

## Model 1

The objective of Model 1 is to explore the first phase of phyllotactic patterning, during which new bract primordia are inserted between previously formed ones within an expanding active ring. The model is expressed using the formalism of L-systems (1–3), which is well suited for simulating circular structures with a changing number of interacting components. Both the primordia and the active ring segments that separate them are represented explicitly as L-system modules arranged into a circular L-system string. A primordium is characterized by its position (arc-length distance from the first primordium modulo the ring perimeter) and age (time elapsed since the primordium creation). A segment is characterized by its state and polarity, corresponding to symbols $\overleftarrow{S}$, $\overleftarrow{L}$ and $\overrightarrow{S}$, $\overrightarrow{L}$ described in the main text. A simulation begins with a small active ring with a single primordium and proceeds by iterating four phases:

1. Expand the active ring,

2. Displace incipient primordia laterally,

3. Insert new primordia into the intervals that exceed threshold length, and

4. Visualize the results.

The active ring expands uniformly, at a constant rate $k_r > 0$. Ring radius $r_a$, which in Model 1 is equal to the distance of the primordia from the ring center, thus increases according to the function

$$\Delta r_a(t) = r_a(t) \cdot k_r \cdot \Delta t,$$

where $\Delta t$ is a time increment per simulation step. Optionally, the threshold length of the active ring segment $Th_l$ into which a new primordium will be inserted is reduced by a predefined factor $k_{Th}$:

$$\Delta Th_l(t) = Th_l(t) \cdot k_{Th} \cdot \Delta t.$$

This reduction allows for simulating the observed decrease of the space into which new primordia are inserted over time.

In the absence of molecular data revealing the mechanism of lateral displacement, we employed a simple heuristic formula to displace an incipient primordium $i$, identified by being younger than both of its neighbors, towards its older neighbor $j$:

$$\Delta d_i(t) = -k_d \cdot (d_{i,j}(t) - d_0(t)) \cdot \Delta t. \qquad [1]$$

**T Zhang, M Cieslak, A Owens, F Wang, SK Broholm, TH Teeri, P Elomaa, and P Prusinkiewicz**

Here $d_{i,j}(t)$ is the arc-length distance between the incipient primordium and its older neighbour, measured along the active ring. Constant $k_d > 0$ and function $d_0(t) > 0$ are model parameters. This equation stipulates attraction of the incipient primordium towards its older neighbor for distances $d_{i,j}(t)$ greater than target distance $d_0$, no interaction for $d_{i,j}(t) = d_0$, and repulsion at distances smaller than $d_0$. Displacement rate $k_d$ controls the magnitude of these influences (Fig. S5 B–D). In all simulations shown we assumed $d_0 = \frac{1}{2}Th_l(t)$, which means that, upon a symmetric insertion, the incipient primordium is neither attracted nor repelled by its neighbors.

A new primordium is inserted into any segment of the active ring that exceeds the current threshold arc length $Th_l$. The primordium divides the ring segment between its younger and older neighbors in proportion $\lambda : (1 - \lambda)$, where the parameter $\lambda \in (0, 1)$ controls the asymmetry of insertion. Consistent with the Hofmeister / Snow and Snow hypothesis and experimental observations suggesting that new primordia are inserted symmetrically (Figs. 4 F, G and Fig. 5 C), we assumed $\lambda = 0.5$ (symmetric division) (Fig. 4 H).

Upon the insertion of a new primordium, the state and polarity of the incident segments are updated according to the age of the neighboring primordia. In addition, existing intervals S change to L. For parameters resulting in a Fibonacci progression of primordia numbers, these transitions are equivalent to L-system productions shown in Fig. 4 E. The model visualizes both the primordia and the intervals between them. Several visualization modes are supported. To facilitate comparisons of the model with reality, the simulation can be shown with experimentally obtained images in the background (Fig. 4 I) and suspended for a predefined time at selected frames to focus on developmental stages of interest (Movie 1). Consecutive states of the simulation can be superimposed to form a single image illustrating the progress of the simulation over time (Fig. S5).

## Model 2

Model 2 extends Model 1 from the early patterning of bracts to the patterning of all primordia. The primordia are no longer confined to the active ring and eventually cover the entire receptacle, abstracted as a flat disk. Correspondingly, primordia configurations are no longer represented by an L-system string with explicitly identified neighbors, but by a set of primordia positions, with the neighbors inferred on the basis of distances.

The radius of the active ring is controlled by a graphically defined function of time, $r_a(t)$ (Fig. S6 A). Consistent with experimental data (Figs. 2 and 6 D–H), this function first increases, capturing ring expansion as in Model 1, then decreases to simulate ring contraction in a later stage of patterning.

A newly created primordium $i = 1, 2, \dots$ lies on the active ring. Over time, its position $r_i(t)$ is updated using the equation:

$$\Delta r_i(t) = r_a(t) \cdot g(t) \cdot \Delta t. \tag{2}$$

The graphically defined function $g(t)$ (Fig. S6 B) specifies changes in the radial position of primordia with respect to radius $r_a(t)$ of the (circular) active ring (under the assumption that $r_a(t) \leq r_i(t)$). Initially $g(t)$ is greater than 0, causing early bract primordia to move centrifugally beyond the active ring. The differences in the radial distances of primordia are at first imperceptible, but increase over time. A sawtooth pattern front results (Fig. 7 A – C). When the active ring starts contracting, $g(t)$ is reduced to 0. The radial coordinate $r_i$ of primordia initiated at this stage thus remains fixed.

To determine when and where new primordia should be inserted, the active ring is sampled in small angular steps ($10^{-4}$ radians in the simulations shown), and distance $d_{i,j}$ of each sample point $i$ to each primordium $j$ is computed as a function of their polar coordinates $(r_i, \phi_i)$ and $(r_j, \phi_j)$ (Fig. S6 D and E):

$$d_{i,j} = \sqrt{(\bar{r}_{i,j}(\phi_i - \phi_j))^2 + (r_i - r_j)^2}. \tag{3}$$

The first term approximates the arc-length distance between points $i$ and $j$, measured along a circle of radius $\bar{r}_{i,j} = (r_i + r_j)/2$ (the average of radii $r_i$ and $r_j$). The second term is the radial distance between points $i$ and $j$. If distance $d_{i,j}$ is above the graphically defined threshold $Th_d(t)$ (Fig. S6 C) for all existing primordia $j$, a new primordium with polar coordinates $(r_i, \phi_i)$ is inserted at sample point $i$ and its two closest neighbors are recorded. If the new primordium is almost at the same distance from three primordia, the younger two primordia are considered the nearest neighbors.

We experimented with several extensions of Eq. 1 to simulate the displacement of incipient primordium $i$ towards its older neighbor $j$ on a disk. The results shown in Fig. 7 and in Movie 2 were obtained by assuming that only the angular component $\phi_i$ of the primordium's position is affected:

$$\Delta \phi_i(t) = -(\cos \alpha \cdot k_d)(\phi_{i,j} - \cos \alpha \cdot \phi_0)\Delta t. \tag{4}$$

Here $\phi_{i,j} = \phi_i - \phi_j$ is the angle between primordia $i$ and $j$, and $\phi_0 = Th_d/\bar{r}$ is the angular counterpart of threshold distance $Th_d$ in Model 1. Coefficient $\cos \alpha$, defined by formula

$$\cos \alpha = \frac{\bar{r} \cdot \phi_{i,j}}{d_{i,j}}, \tag{5}$$

reduces the displacement rate $k_d$ and the angular rest distance $\phi_0$ when radial positions $r_i$ and $r_j$ differ. Graphically, only projections of these values on (a tangent to) the active ring are considered (Fig. S6 E).

In Movie 2, primordia are initially displayed as circles with radii indicating current threshold $Th_d(t)$, then as spheres approximating the actual primordium size. This transition makes it possible to visualize both the interaction between primordia on the active ring and their subsequent self-organization into a circular lattice.

## Model 3

Model 3 simulates phyllotactic patterning on a data-driven model of the gerbera receptacle. It is an extension of Model 2 to a continuously growing, curved surface. The simulation begins with a small receptacle and proceeds by iterating the same phases as Models 1 and 2. In contrast to those models, however, the expansion of the receptacle and advancement of the active ring are determined by data extracted from microscopic observations.

**The dynamic receptacle model.** The model describes the receptacle as its size and shape change in the course of head development. In addition, it characterizes trajectories of material points on the receptacle surface due to nonuniform growth. The receptacle is modeled as a polygonized surface of revolution, obtained by rotating a growing profile curve around the head axis (4, 5). The profile curve is modeled as a B-spline (6, 7). B-spline approximation techniques are used twice: first to fit individual profile curves to data points obtained by digitizing a sequence of head sections, then to create a continuous-time progression between these curves.

The input consists of volumetric data representing $K = 11$ heads at different developmental stages (Fig. 2 A). We extracted a longitudinal section of each head using MorphoGraphX (8), and combined these sections into a composite image using Photoshop (Fig. S9 A). We then fitted a uniform cubic B-spline to the right half of each receptacle using the method described before in the context of leaf contour tracing (9). Each profile was thus represented by a parametric curve $C_k : [0, 1] \to \mathbb{R}^2$ of the form

$$C_k(s) = \sum_{i=0}^{I_k} B_{3,i}(s) P_{i,k},$$

where $s$ is the normalized ($s \in [0, 1]$) arc-length position along the curve, $k = 1, 2, \ldots, K$ is the profile number, $I_k$ is the number of control points, $P_{i,k}$ are 2D positions of the control points, and $B_{3,i}(s)$ are B-spline basis functions of degree three. The curves were clamped to the interval $[0, 1]$ by replicating knots four times at its beginning and end.

To simulate receptacle growth continuously over time, we blended profiles $C_k(s)$ using quadratic B-splines $B_{2,k}$:

$$C(t, s) = \sum_{k=1}^{K} B_{2,k}(t) C_k(s). \tag{6}$$

The resulting head profiles (curves $t = \text{const}$) and trajectories of points with the same normalized arc-length parameter (curves $s = \text{const}$) are shown in Fig. S9 B. As our data did not include the age of the sample heads, we manually adjusted positions of the spline knots that control progression through the blending functions over time (Fig. S9 C) to approximate smooth growth of the simulated head.

To simulate the trajectories of materials points, we tracked visible primordia in the composite image of head sections, treating them as landmarks embedded in the developing head (10). The landmarks in profile $k$ were numbered from $j = 1$ (closest to the base) to $j = J_k$ (closest to the apex), and their positions $s_{j,k}$ were expressed in terms of the normalized arc-length parameter $s$. The base and the apex of each profile were treated as additional landmarks, $s_{0,k} = 1$ and $s_{J_k+1,k} = 0$. As younger heads had fewer landmarks than older ones, we propagated missing landmarks from older to younger profiles by assuming that profile segments with no landmarks expand uniformly in length. For example, a landmark $s_{j+1,k}$ appearing on profile $k$ but not on profile $k - 1$ is propagated by evaluating the following equation:

$$\frac{s_{j+1,k-1}}{s_{j,k-1}} = \frac{s_{j+1,k}}{s_{j,k}}.$$

Fig. S9 D shows how this landmark is propagated in the context of existing landmarks.

Given the landmarks, we constructed a continuous mapping of material point coordinates $w$ to normalized arc-length parameters $s$ in profile $k$:

$$s_k(w) = \sum_{j=0}^{J_k+1} B_{2,j}(w) s_{j,k},$$

and blended all profile mappings to express $s$ over continuous time $t$:

$$s(t, w) = \sum_{k=1}^{K} B_{2,k}(t) s_k(w).$$

By substituting $s(t, w)$ for the arc length $s$ in Eq. 6 we re-expressed the profile curves in terms of material points $w$:

$$\widehat{C}(t, w) = C(t, s(t, w)).$$

The resulting reparametrization describes the trajectories of material points over time (curves with constant $w$) while maintaining head profiles captured by Eq. 6 (curves with constant $t$) (Figs. 8 A and S9 E).

The final component of the receptacle model characterizes the positions of the active ring. We estimated its normalized arc-length position $s_{a,k}$ in each profile $k = 1, \ldots, K$ from the position of the youngest visible primordium. As patterning of

**T Zhang, M Cieslak, A Owens, F Wang, SK Broholm, TH Teeri, P Elomaa, and P Prusinkiewicz**

auxin maxima precedes morphological changes in the receptacle (Fig. 3), we assumed that the active ring lies ahead of this primordium, separated from it by approximately four (still invisible) incipient primordia. We then fitted a spline to obtain a continuous representation of the active ring's position over time:

$$s_a(t) = \sum_{k=1}^{K} B_{2,j}(t) s_{a,k}.$$

Given Eq. 6, the curve describing the position of the generative zone over time is thus

$$G(t) = C(t, s_a(t)).$$

We have modeled the shape of the growing receptacle, the propagation of material points, and the propagation of the active ring on its surface by rotating profiles and trajectories captured by functions $\widehat{C}(t, w)$ and $G(t)$ around a vertical axis (Fig. 8 B and Movie 3).

**Phyllotactic patterning on the receptacle.** The position of the active ring on the receptacle is given by function $s_a(t)$ in the case of a circular active ring (Fig. 9 C and Movies 4 and 5). To model an elliptic ring (Fig. 9 E and Movie 6), we assumed that the arc-length coordinate $s_e$ of a point on the ring varies with its polar coordinate $\phi$ according to the function

$$s_e(t, \phi) = s_a(t) + A \cdot \min(r_1(t) - r_a(t), r_a(t)) \cdot \sin(2(\phi - \phi_{ref})).$$

Parameter $A \geq 0$ controls the eccentricity of the ellipse. Variable $r_1(t)$ is the current radius of the receptacle, assumed to be equal to the distance from the disk center to the oldest primordium. The term $\min(r_1(t) - r_a(t), r_a(t))$ modifies the eccentricity as a function of the ring size. The maximum eccentricity is thus reached in the middle of the receptacle, where $r_a = \frac{1}{2} r_1$. Parameter $\phi_{ref}$ controls the inclination of the ellipse. The simulation in Fig. 9 E was performed assuming $A = 2 \times 10^{-3}$ and $\phi_{ref} = 140°$.

A newly created primordium lies on the active ring such that its arc-length position $s_i(t)$ equals $s_a(t)$ (or $s_e(t)$) at the time of insertion. A primordium's position over time is updated by evaluating $s_i(t) = s(t, w_i)$, where $w_i$ is the material coordinate of the primordium. The ages and radii of primordia are updated as in Model 2. New primordia are inserted when and where there is enough space for them on the active ring. The distance between each primordium $i$ to sample point $j$ on the ring is computed as:

$$d_{i,j} = \sqrt{\left(\frac{r_i + r_j}{2}(\phi_i - \phi_j)\right)^2 + (L(t) \cdot (s_i(t) - s_j(t)))^2}, \tag{7}$$

where $L(t)$ is the length of the profile curve $C(t, s)$ (recall that arc-length distance $s$ is assumed to be normalized). The difference in angular position is thus computed as in Model 2, but the difference in radial position is replaced by the difference in arc-length position. The lateral displacement is computed using Eqs. 4 and 5, with distance $d_{i,j}$ between primordia calculated using Eq. 7 instead of Eq. 3. Simulation results are shown in Fig. 8 C and Movies 4–6.

**The dynamic primordium model.** To enhance the visual realism of the phyllotaxis model, we extended it with a three-dimensional submodel of floret primordia, informed by the description of their development (11). Ray, trans and disk florets are considered jointly, as their differences only appear later, outside the model time range. Bracts are modeled schematically, as elliptical bumps, because longitudinally extended bracts would obscure the receptacle.

At each point in time, the model takes as input the position $p$ and boundary $B$ of each primordium. It returns the shape of each primordium as a height function: displacement from the reference receptacle surface $S$ in the normal direction. To facilitate computation, we locally approximate the receptacle surface $S$ near each primordium by the tangent space $T_p S$ centered at the primordium center $p$.

We modeled the first four stages of floret primordium development (11), whereby its distinct physical appearance characterizes each stage (Fig. S10 K). At Stage 1, floret primordia continuously deform from a flat area of the receptacle to an undifferentiated bump. Each bump begins to form ring-shaped petals at Stage 2, with the center depressing slightly and a ridge rising along the periphery. Individual petals emerge at Stage 3, usually in a five-fold radially symmetric pattern; on occasion, we have observed six petals in nature. At Stage 4, petals elongate, covering the developing stamen and carpel primordia; however, we did not model these covered structures. The model has two components: a model of isolated floret primordia, which ignores the influence of their neighbors, and a model of primordia deformation, which captures the effect of primordia crowding (tight packing) on the receptacle.

Isolated primordium model. To model an isolated primordium, the primordium boundary $B$, approximated as an ellipse, is transformed to the tangent space $T_p S$ and approximated as circle $B'$ (Fig. S10 A and B). This transformation is effected using the normalized distance function

$$\rho(q) = \frac{(u_q - u_p)^2}{a^2} + \frac{(v_q - v_p)^2}{b^2},$$

where $(u_p, v_p)$ are Cartesian coordinates of the primordium center $p$, $(u_q, v_q)$ are the corresponding coordinates of an arbitrary sampling point $q$, and parameters $a$ and $b$ are semi-axes of the ellipse.

We use height function $f_{bump\_contour}(\rho)$ to model the undifferentiated bump in Stage 1 and the overall contour of the primordia in the subsequent developmental stages. The emergence of the bump is modeled as a function of age, which scales the contour shape (Fig. S10 C):

$$f_{bump}(\rho, age) = f_{height}(age)f_{bump\_contour}(\rho).$$

In Stage 2, the primordium shape is transformed into a cylinder with an elevated ridge on the perimeter. This transformation is captured by modifying the shape of the bump using function $f_{ridge\_contour}(\rho)$ (Fig. S10 D):

$$f_{ridge}(\rho, age) = f_{bump}(\rho, age)f_{ridge\_contour}(\rho).$$

Primordia in Stages 3 and 4 have an emergent corolla with $n = 5$ or $n = 6$ petals. To model it, we first define a star-shaped stencil in tangent space $T_pS$ (Fig. S10 E):

$$f_{corolla\_stencil}(\rho, \theta, age) = \quad f_{petal\_spacing}(age)\left(\cos\left(\frac{n\theta}{4}\right)^{-\frac{3}{2}} + \sin\left(\frac{n\theta}{4}\right)^{-\frac{3}{2}}\right)^{\frac{1}{2}} - \rho.$$

Points satisfying the inequality $f_{corolla\_stencil}(\rho, \theta, age) \leq 0$ represent petals; the remaining points are indentations between them. The size of petals is controlled by the graphically defined function $f_{petal\_spacing}$. Given $f_{corolla\_stencil}$, the three-dimensional primordium shape is defined as the height function (Fig. S10 F):

$$f_{petals}(\rho, \theta, age) = \quad \begin{cases} f_{bump}(\rho, age) & \text{if } f_{corolla\_stencil}(\rho, \theta, age) \leq 0, \\ f_{bump}(\rho, age)f_{indentation\_depth}(\rho) & \text{otherwise.} \end{cases}$$

The function $f_{indentation\_depth}(\rho)$ controls the depth of indentation between the petals.

The final shape $f_{floret}$ of an isolated primordium is a weighted combination of shape functions $f_{bump}$, $f_{ridge}$ and $f_{petals}$:

$$f_{floret}(\rho, \theta, age) = \alpha(age)f_{bump}(\rho, age) \ + \beta(age)f_{ridge}(\rho, age) \ + \gamma(age)f_{petals}(\rho, \theta, age).$$

The weight functions $\alpha$, $\beta$, and $\gamma$ are defined graphically (Fig. S10 J), and are guaranteed to sum to unity via normalization.

Inter-primordium collisions. The phyllotaxis model produces a tightly packed patterning of primordia, each demarcated by their boundary $B$. The boundaries produced from the model are elliptical by construction. However, there are stages of primordium growth (e.g., between stages 1 and 3) that do not have elliptical boundaries (11). The radial size of these primordia appear larger than the available space relative to their neighboring primordia and therefore must deform. The resultant pattern of primordia is tightly packed, conforming to the collisions between primordia. We model the available space of colliding primordia as the Voronoi diagram of the primordium positions $p$ on the surface $S$ (Fig. S10 G) (a detailed review of Voronoi diagrams can be found in (12)). If the primordium's boundary $B'$ exceeds the available space demarcated by its Voronoi cell, then the primordium is deformed to fit within the Voronoi cell (Fig. S10 H). We model the primordium's shape at sample point $q$ via the shape function $f_{floret}(\rho, \theta, age)$, however, we fit this shape into the available space of the Voronoi cell (i.e., primordia neighborhood) by scaling the distance value ($\rho$) smoothly towards 1 as $q$ approaches the Voronoi cell's boundary $\partial V_p$. Therefore, the scaling factor must map $\rho$ such that 1) it is a function of $q$'s position within the Voronoi cell, 2) it preserves the distance $\rho$ in the interior of the Voronoi cell, and 3) it smoothly maps $\rho$ to 1 near the boundary $\partial V_p$. We construct this distance remapping function $f_{Voronoi}$ in two parts: first, we compute a smooth, monotonically increasing, shape-aware scalar field over the domain of the Voronoi cell $V_p$; second, we remap this scalar field via a graphically defined function that controls the shape and speed of the fall-off towards the Voronoi cell boundary $\partial V_p$.

*Computing Voronoi diagram.* The Voronoi diagram is calculated in 2 steps from the primordia positions (i.e., centers). First, we use a 3D surface construction algorithm (13) to construct the Delaunay triangulation of primordia centers. Second, we calculate the dual graph of the Delaunay triangulation. The Voronoi diagram partitions the surface $S$ into Voronoi cells (polygons). Each Voronoi cell $V_p$ encloses a single primordium position $p$ (Fig. S10 G). The boundary $\partial V_p$ comprises several linear segments; each segment is shared with the boundary of a neighboring primordium (e.g., $\partial V_{p'}$), and is equidistant from $p$ and $p'$.

*Computing the interior of a Voronoi cell.* We desire a scalar function $f$ over the (two-dimensional) domain of the Voronoi cell $V_p$ that is smooth and monotonically increasing from the center $p$ outwards to the boundary of the Voronoi cell $\partial V_p$, such that $f$ evaluates to 0 at $p$, and $f$ evaluates to 1 on the boundary $\partial V_p$. The function $f$ is easily modeled as a boundary value problem—a partial differential equation with appropriate boundary conditions. The unique solution to Laplace's equation is such a function

$$\nabla^2 f\big|_{V_p} = 0,$$

subject to the Direchlet boundary conditions

$$f\big|_p = 0,$$
$$f\big|_{\partial V_p} = 1.$$

**T Zhang, M Cieslak, A Owens, F Wang, SK Broholm, TH Teeri, P Elomaa, and P Prusinkiewicz**

We solve this equation numerically over a rectilinear grid obtained by discretizing domain $V_p$ in the tangent space $T_pS$. The discrete vertical and horizontal spacing between grid points ($\Delta u$ and $\Delta v$, respectively) are fractions of the linear coordinates in the tangent space at $p$ (Fig. S10 H). The values of $f$ over $V_p$ are therefore multiples of the vertical and horizontal spacing, i.e.,

$$f_{i,j} = f(i\Delta u, j\Delta v),$$

where $i, j \in \mathbb{Z}$. The Laplacian operator ($\nabla^2$) applied to $f$ evaluated over $T_pS$ is then approximated via the central finite difference

$$\nabla^2 f(u,v) = \frac{\partial^2 f}{\partial u^2} + \frac{\partial^2 f}{\partial v^2} \approx \frac{f_{i-1,j} - 2f_{i,j} + f_{i+1,j}}{(\Delta u)^2} + \frac{f_{i,j-1} - 2f_{i,j} + f_{i,j+1}}{(\Delta v)^2},$$

and the Laplace equation becomes

$$\nabla^2 f(u,v) \approx \frac{f_{i-1,j} - 2f_{i,j} + f_{i+1,j}}{(\Delta u)^2} + \frac{f_{i,j-1} - 2f_{i,j} + f_{i,j+1}}{(\Delta v)^2} = 0.$$

We rearrange the equation to solve for $f_{i,j}$

$$f_{i,j} = \frac{(\Delta v)^2 \left(f_{i-1,j} + f_{i+1,j}\right) + (\Delta u)^2 \left(f_{i,j-1} + f_{i,j+1}\right)}{2(\Delta u)^2 + 2(\Delta v)^2}, \tag{8}$$

which implies the solution to the Laplace equation at $f_{i,j}$ is in terms of $f$ evaluated at neighboring grid points. Given initial values of $f_{i,j}|_{V_p}$, and the (Dirichlet) boundary conditions $f(p) = f_{0,0} = 0$, and $f_{i,j}|_{\partial V_p} = 1$, we iteratively solve the Laplacian equation (Eq. 8) for each $f_{i,j}^k$,

$$f_{i,j}^{k+1} = \frac{(\Delta v)^2 \left(f_{i-1,j}^k + f_{i+1,j}^k\right) + (\Delta u)^2 \left(f_{i,j-1}^k + f_{i,j+1}^k\right)}{2(\Delta u)^2 + 2(\Delta v)^2},$$

for $k = 0, 1, 2, \ldots$ until the function converges to within some tolerance $\epsilon$; i.e., $|f_{i,j}^{k+1} - f_{i,j}^k| < \epsilon$ for all $i$ and $j$.

*Scaling the distance.* The solution to Laplace's equation is a scalar field over the domain $V_p$, the values of which increase smoothly and monotonically from the primordium center towards the domain boundary. We use a graphically defined function to remap these values to a scaling factor that is applied to the radial distance $\rho$ of any point $q = (u_q, v_q) \in V_p$. The scaling factor maps $\rho$ towards a distance of 1 (where $f_{floret}$ falls off) as $q$ approaches the boundary of the Voronoi cell $V_p$ (Fig. S10 G and H) . The shape of the primordium is preserved at any developmental stage, albeit now conforming to the boundary of the Voronoi cell $\partial V_p$ (Fig. S10). Taking into account the developmental stage (Fig. S10 J), the simulated primordium (Fig. S10 K) can now be incorporated into the final head (Figs. 8 D, 9 K and Movie 7).
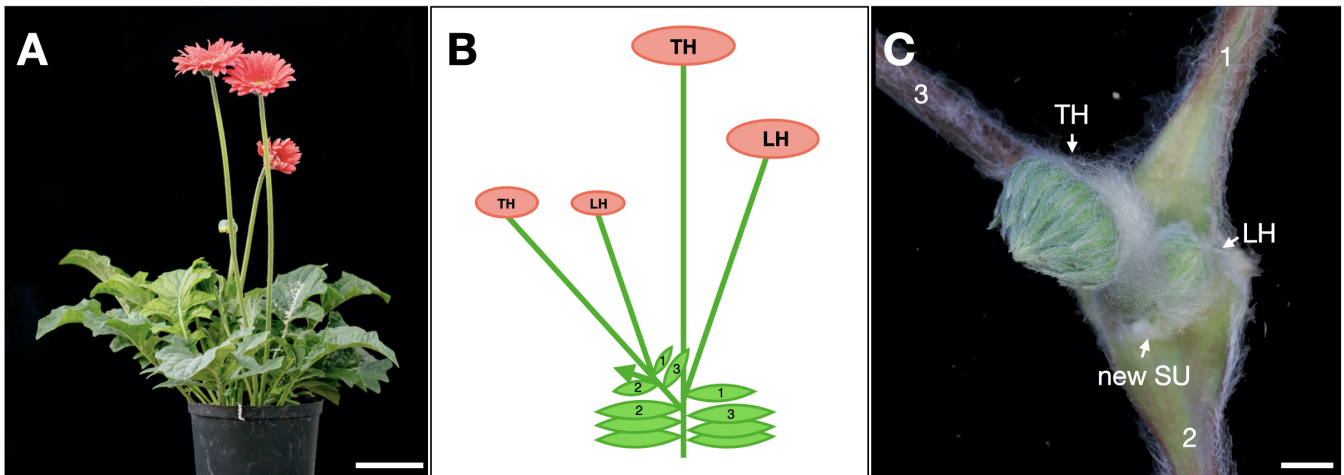
**Fig. S1.** Plant architecture of *Gerbera hybrida*. (A) Side view of a gerbera plant. Flower heads are supported by leafless scapes (stems), which separate them from the rosette leaves. (B) Schematic representation of the plant architecture. A shoot terminates with one terminal head (TH) and one lateral head (LH) initiated in the axil of the youngest leaf (1). A new shoot continues from the axil of the second youngest leaf (2). C) Top view of a dissected gerbera shoot showing three leaves (1, 2, 3), two flower heads (TH, LH), and a new shoot (new SU) corresponding to the schematic drawing in (B). Scale bars: 10 cm (A), 1 cm (C).

**T Zhang, M Cieslak, A Owens, F Wang, SK Broholm, TH Teeri, P Elomaa, and P Prusinkiewicz**

## TR3

Auxin          Mock

## TR7

Auxin          Mock

## TR5

Auxin          Mock

## TR8

Auxin          Mock
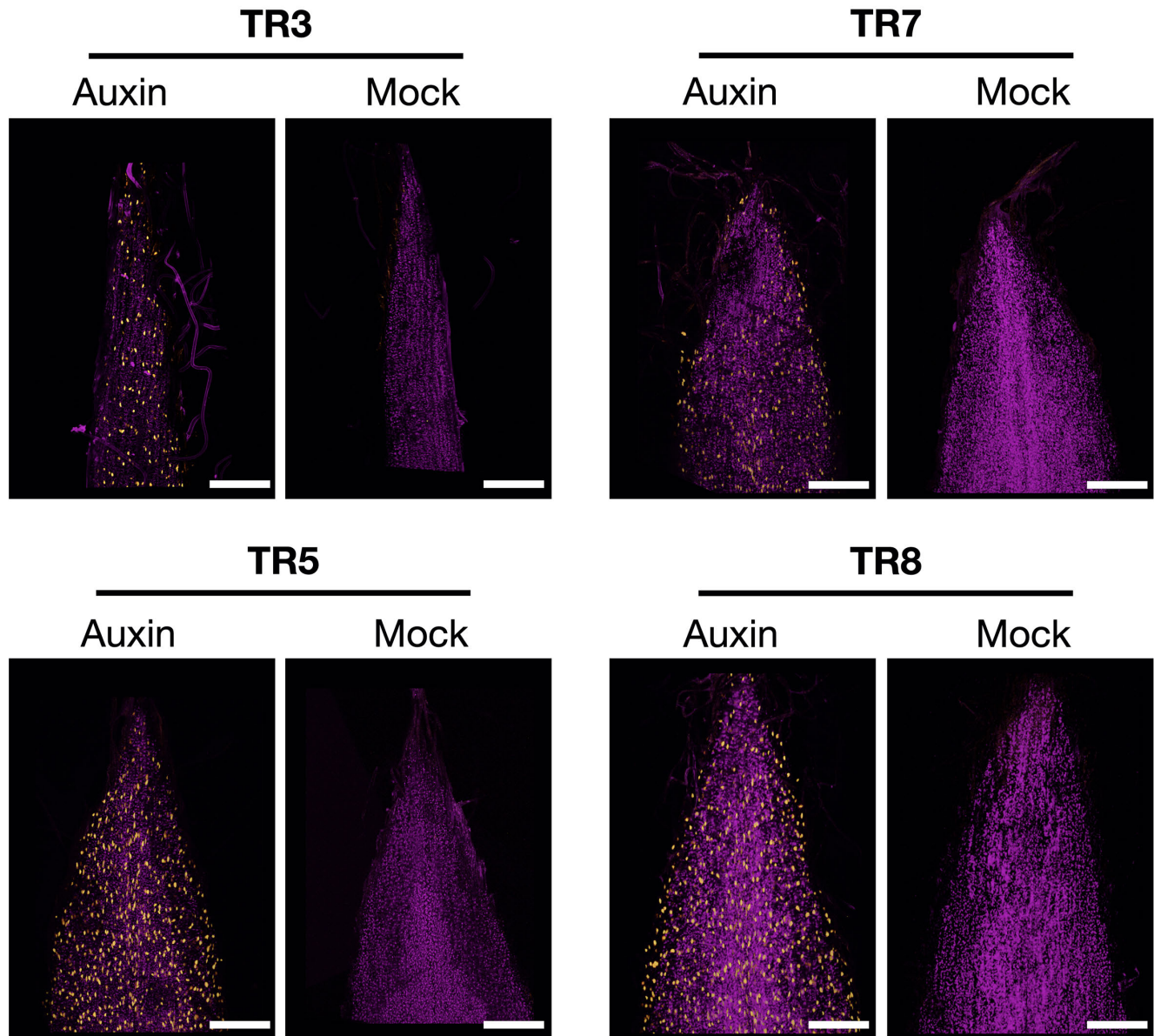
**Fig. S2.** The response of gerbera DR5rev:3xVENUS-N7 reporter lines to auxin treatment. Confocal microscopic images show top projections of the adaxial epidermis in bracts detached from 3-4 mm flower heads. The images were collected 12 hours after submerging the dissected bracts into auxin (10 $\mu$M IAA + 10 $\mu$M NAA) or mock solutions. The DR5 signal is shown in yellow, chlorophyll autofluorescence in purple. All four transgenic lines (TR3, TR5, TR7 and TR8) used in this study are responsive to the exogenous auxin, as suggested by the strong DR5 expressions in the treatment group. Scale bars: 200 $\mu$m.
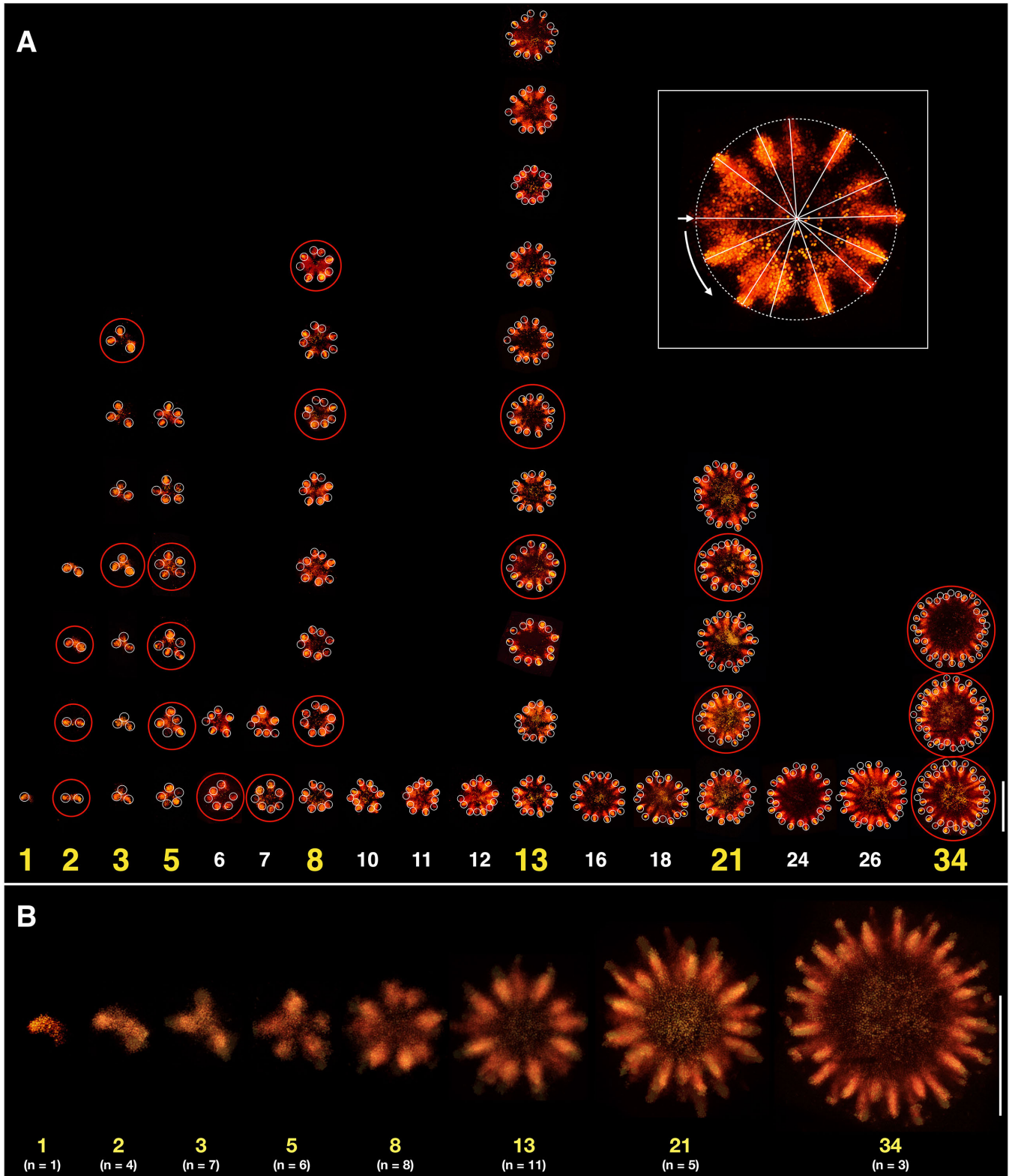
**Fig. S3.** The data set for early patterning of bracts. (A) top view of 56 randomly sampled head meristems with up to 34 auxin maxima, visualized by confocal microscopy. The images of heads marked by the red circles have been reflected to match the chirality of the remaining heads. The inset shows how the angular distances between DR5 maxima have been estimated in Fig. 4 B, counterclockwise from initium 1 (arrows). (B) Superimposed images of multiple heads with the same number of DR5 maxima show that the pattern progression is stereotypical. Scale bars: 500 $\mu$m (A), 200 $\mu$m (B).

**T Zhang, M Cieslak, A Owens, F Wang, SK Broholm, TH Teeri, P Elomaa, and P Prusinkiewicz**
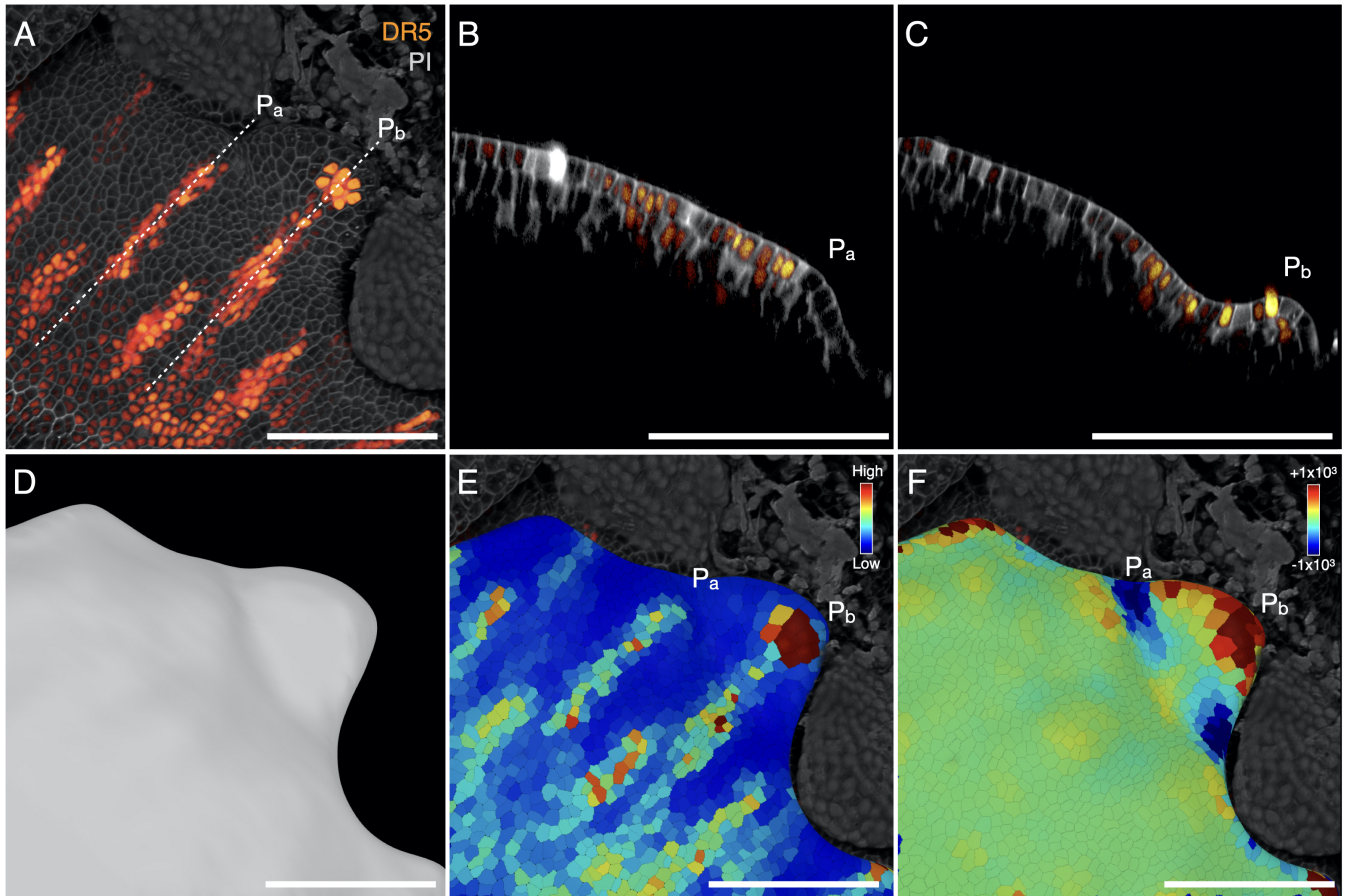
**Fig. S4.** Position of bulging bract primordia in relation to the DR5 signal. (A) Confocal microscopic image showing a sector of the head margin. The head is approximately at stage IV–V identified in Fig. 2. Cell walls are stained with propidium iodide (PI). (B,C) Optical cross section showing outgrowth of primordia $P_a$ and $P_b$. (D) Meristem surface corresponding to image (A) isolated and visualized using MorphoGraphX. (E) DR5 signal intensity of epidermal cells projected on the segmented meristem surface. (F) Gaussian curvature of the meristem surface. Scale bars: 100 $\mu$m.
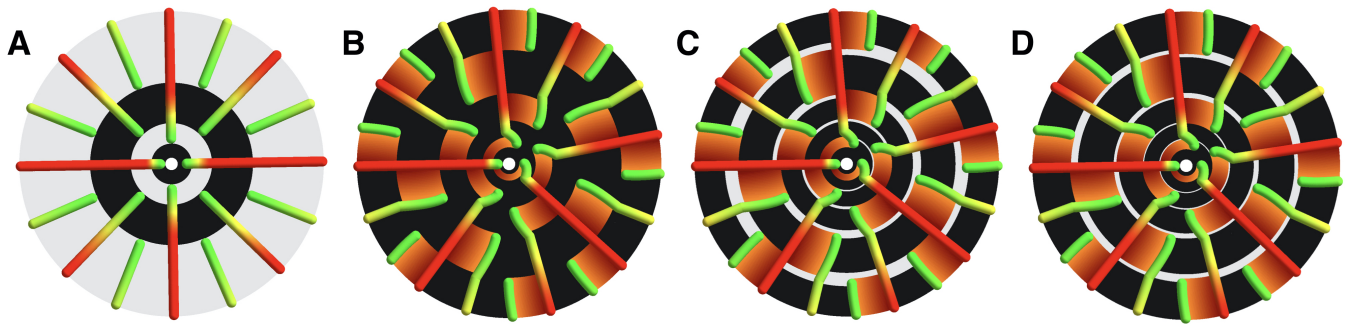
**Fig. S5.** Lateral propagation yields robust progression through Fibonacci primordia numbers in the circle model. (A) Traces of hypothetical primordia (green to red: incipient to older) that emerge symmetrically between their neighbors in an expanding active ring. Primordia numbers increase in a geometric progression (1,2,4,8,...). (B) Traces of primordia that emerge symmetrically and propagate laterally with displacement rate $k_d$ = 0.02025, resulting in strict progression through Fibonacci primordia numbers (See Eq. 1 in Supplementary Text for the definition of parameter $k_d$). (C,D) Traces of primordia for rate $k_d$ reduced by 20% (C) and increased by 20% (D). Dark background zones indicate states with Fibonacci primordia numbers, which occur (A to D): 37.7%, 100%, 82.3%, and 89.3% of time.
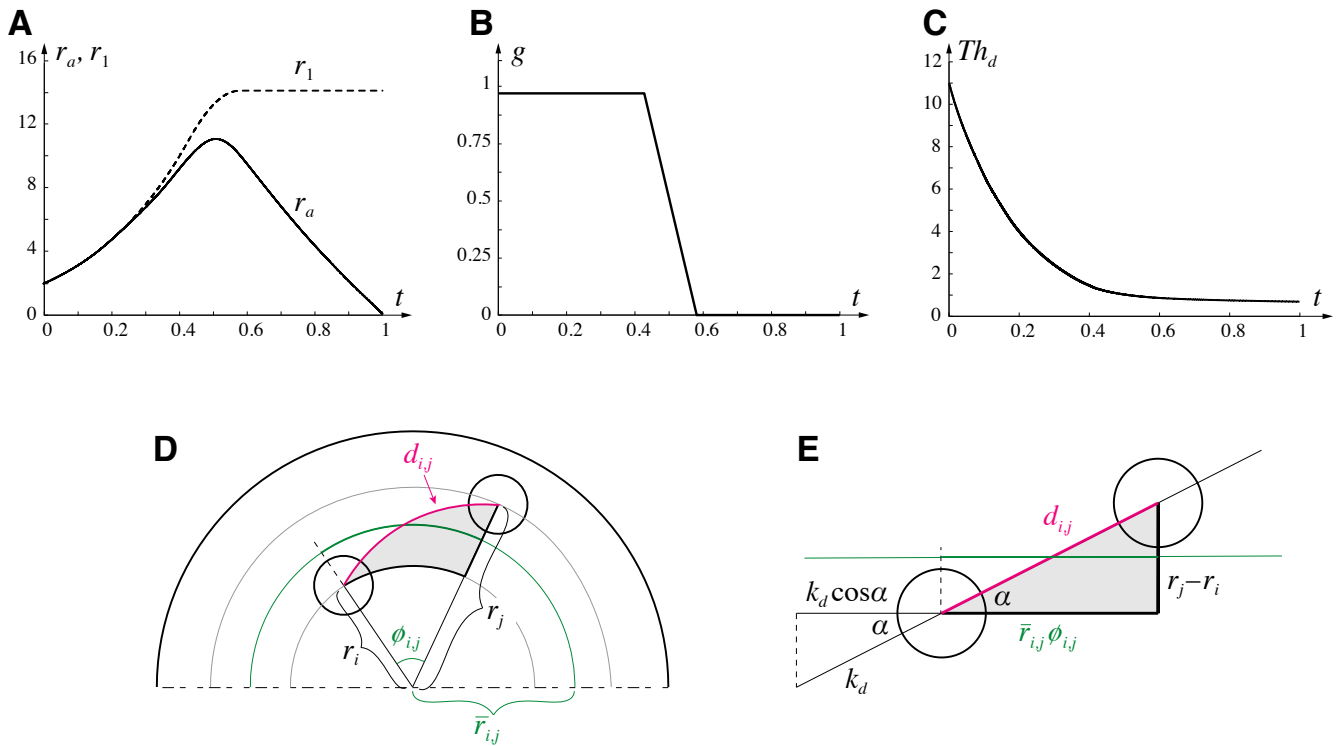
**T Zhang, M Cieslak, A Owens, F Wang, SK Broholm, TH Teeri, P Elomaa, and P Prusinkiewicz**

**Fig. S6.** Elements of Model 2. (A–C) Graphically defined functions controlling the model over normalized development time. (A) Radius $r_a$ of the active ring. (B) Normalized function $g$ controlling receptacle expansion. Dashed line in (A) shows receptacle radius $r_1$ (equal to the distance of the first primordium to the receptacle center) resulting from the combination of functions $r_a(t)$ and $g(t)$ (Eq. 2 in Supplementary Text). (C) Threshold distance $Th_d$ for inserting new primordia. (D,E) Definition of distance between primordia. (D) Distance $d_{i,j}$ between primordium or sampling point $i$ and primordium $j$ is a function of their radial and angular positions. (E) The distance is calculated using a straight-line approximation of the curvilinear geometry in (D). The rate of lateral displacement $k_d$ of incipient primordium $i$ is projected on the tangent to the active ring.
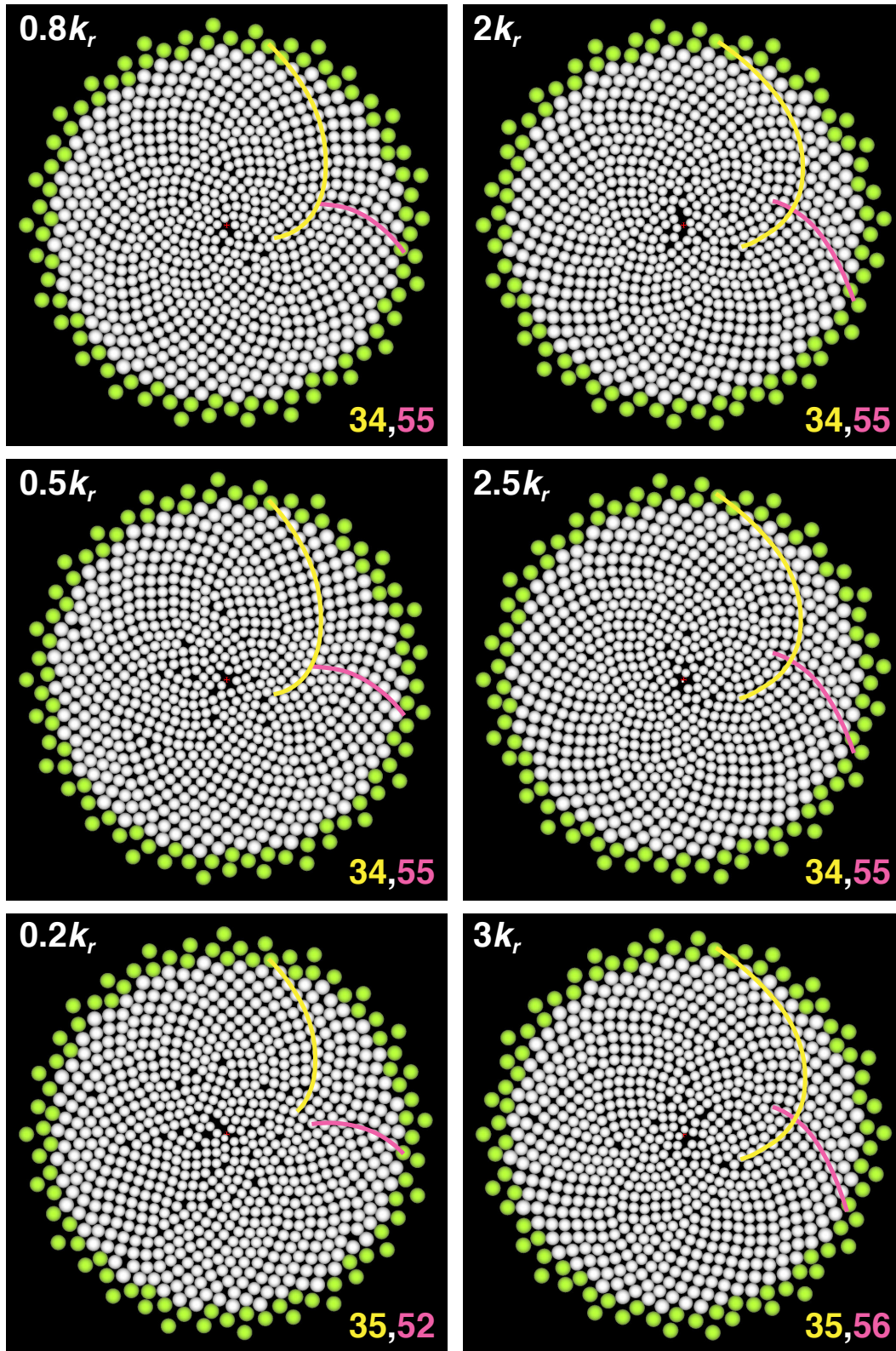
**Fig. S7.** Impact of the lateral displacement rate $k_d$ on patterns generated using Model 2. The rates are shown in proportion to the reference value $k_r$ used in the simulations in Fig. 7.

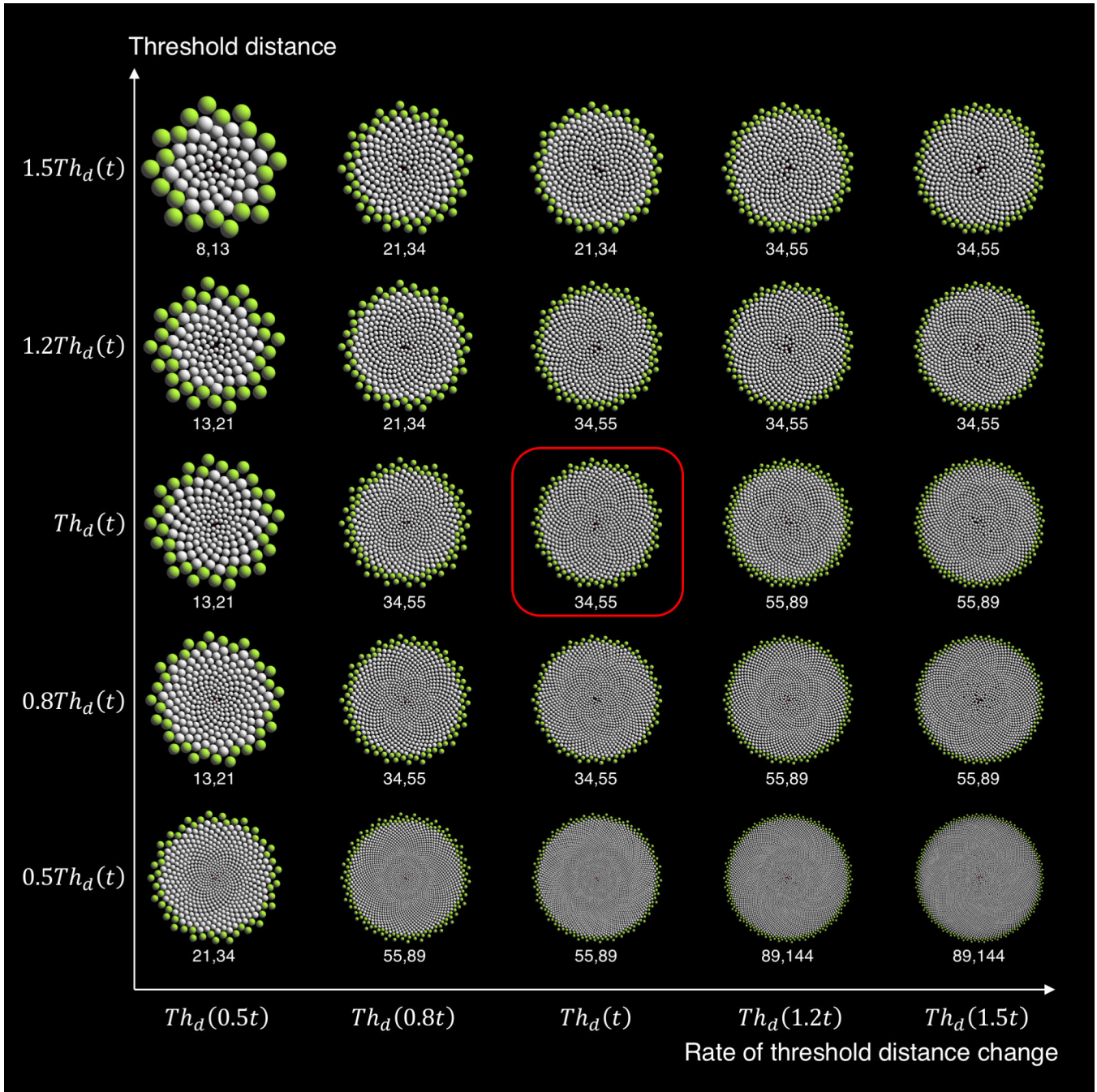T Zhang, M Cieslak, A Owens, F Wang, SK Broholm, TH Teeri, P Elomaa, and P Prusinkiewicz

**Fig. S8.** Impact of the threshold distance to neighbors on the patterns generated using Model 2. Red box indicates the pattern generated using the reference function $Th_d$ defined in Fig. S6 C (same as in Figure 7 D–F up to primordia colors). The remaining patterns result from scaling the values and the rate of change of $Th_d$.
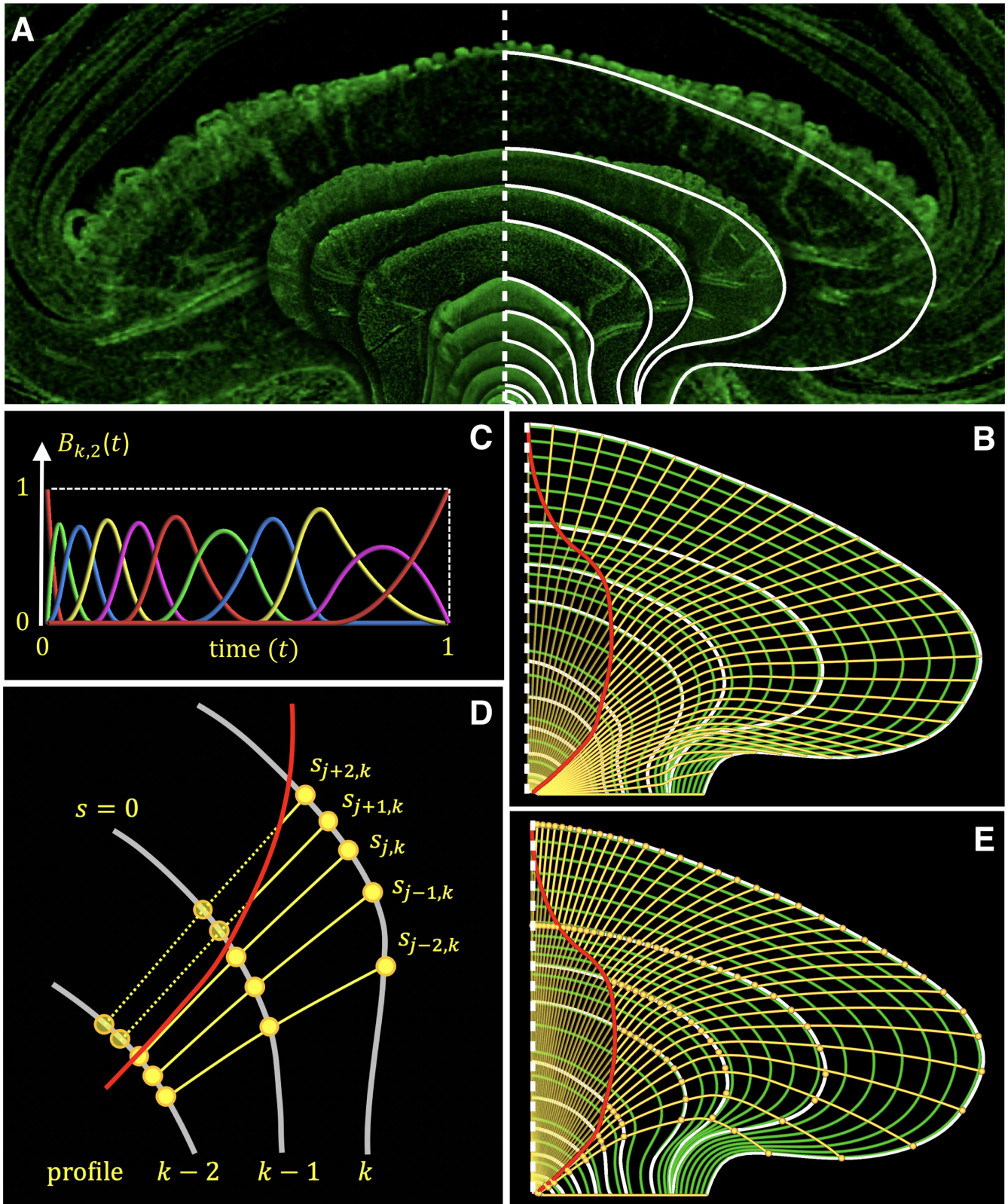
**Fig. S9.** Construction of the dynamic gerbera receptacle model. (A) Longitudinal head sections (corresponding to Fig. 2 A), with interiors suppressed for clarity, are combined into a single image. The receptacle profiles (white curves) are traced manually on one side of the heads. (B) The initial model. Green curves approximate head profiles between the traced stages. Yellow curves show the default trajectories of material points, obtained by assuming that the profiles grow uniformly in length. The red curve represents propagation of the active ring, estimated from the position of the youngest visible primordium at each time point. (C) The quadratic spline functions used as weights to combine consecutive profiles in (B). (D) Method for tracking primordia $s_{j,k}$ (filled circles) that serve as landmarks to estimate local growth rates. Growth of the central domain, where the landmarks are absent, is calculated by extrapolating later growth stages (dotted lines). (E) Dynamic model of the head accounting for the non-uniform growth of its surface (corresponding to Fig. 8 A). Trajectories of material points (yellow curves) are changed with respect to the initial model (B).
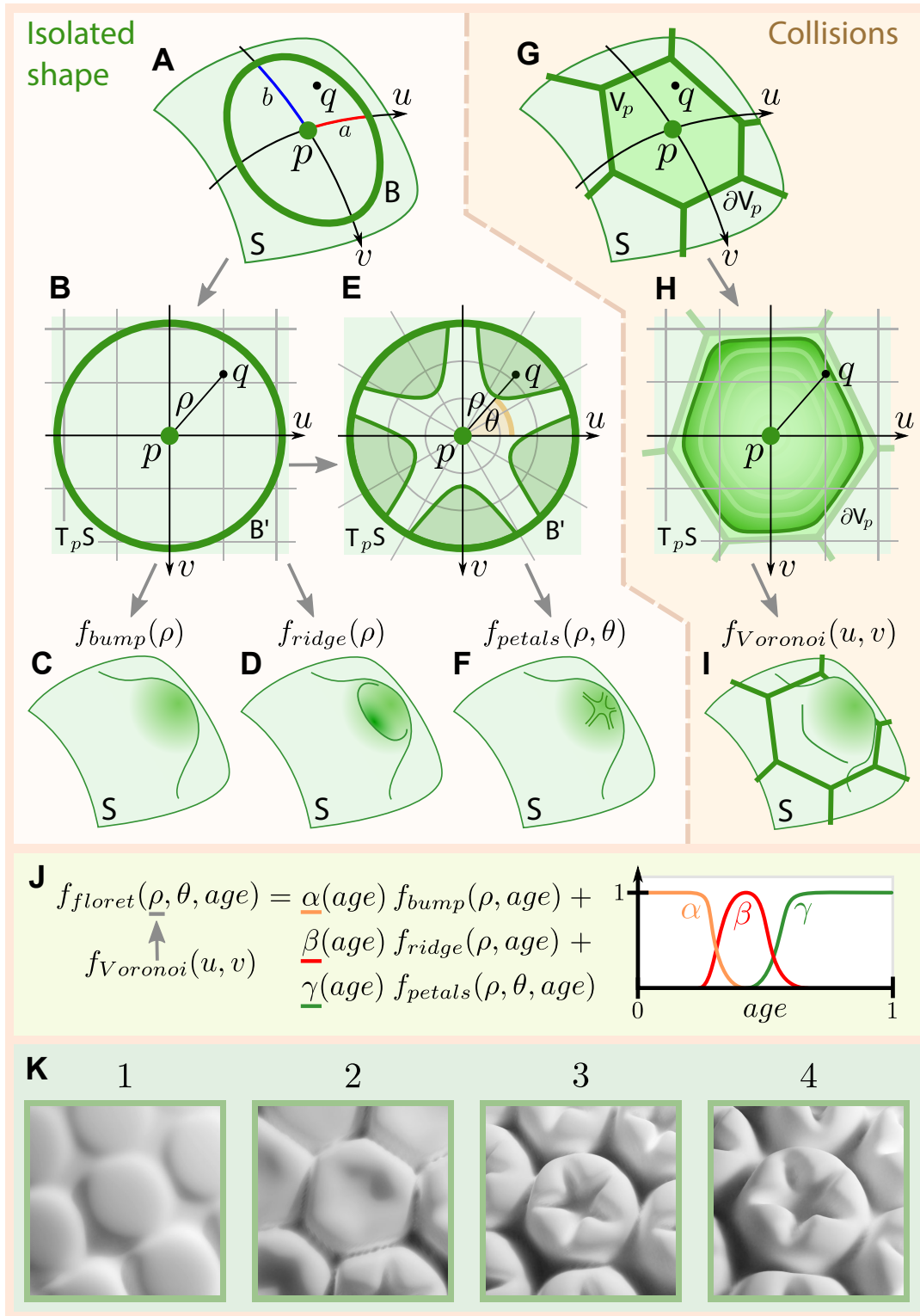
**T Zhang, M Cieslak, A Owens, F Wang, SK Broholm, TH Teeri, P Elomaa, and P Prusinkiewicz**

**Fig. S10.** Construction of the dynamic primordium model. (A) The base of a primordium isolated from its neighbors is embedded in receptacle $S$ characterized by center $p$ and elliptic boundary $B$ with semi-axes $a$ and $b$. (B) The boundary $B$ is transformed to the tangent space $T_pS$ of $S$, centered at $p$. The transformed boundary $B'$ is a circle. (C, D) Early stages of the primordium development are approximated using height functions $f_{bump}$ and $f_{ridge}$ defined on the radial position $\rho$ defined on the tangent plane (C) and transformed back to the receptacle space $S$ (D). (E, F) Later stages of the development are modeled using a stencil (dark and light regions in (E)), which modifies height function $f_{petals}$ according to the polar coordinates $(\rho, \theta)$ to simulate the emergence of petals (F). (G) Information on the primordium neighborhood is encapsulated as a Voronoi cell $V_p$ centered at $p$. The cell is part of a Voronoi diagram, computed by taking into account the centers of all primordia present. (H) Cell $V_p$ is transformed to the tangent space $T_pS$. The isolated primordium base with boundary $B'$, which may extend beyond the Voronoi cell, is deformed to fit within the cell. (I) The deformation, expressed as function $f_{Voronoi}$ that modifies distances to the primordium center, is applied to the height function defining the floret shape. (J) The final floret shape is modeled as a linear combination of the shape functions $f_{bump}$, $f_{ridge}$ and $f_{petals}$. Their relative contributions (weights) are graphically defined functions of the primordium's age, describing the progression of floret shape through developmental stages. The resulting function $f_{floret}$ is modified by function $f_{Voronoi}$ to take the presence of primordium neighbors into account. (K) Snapshots of the simulation of primordium development.
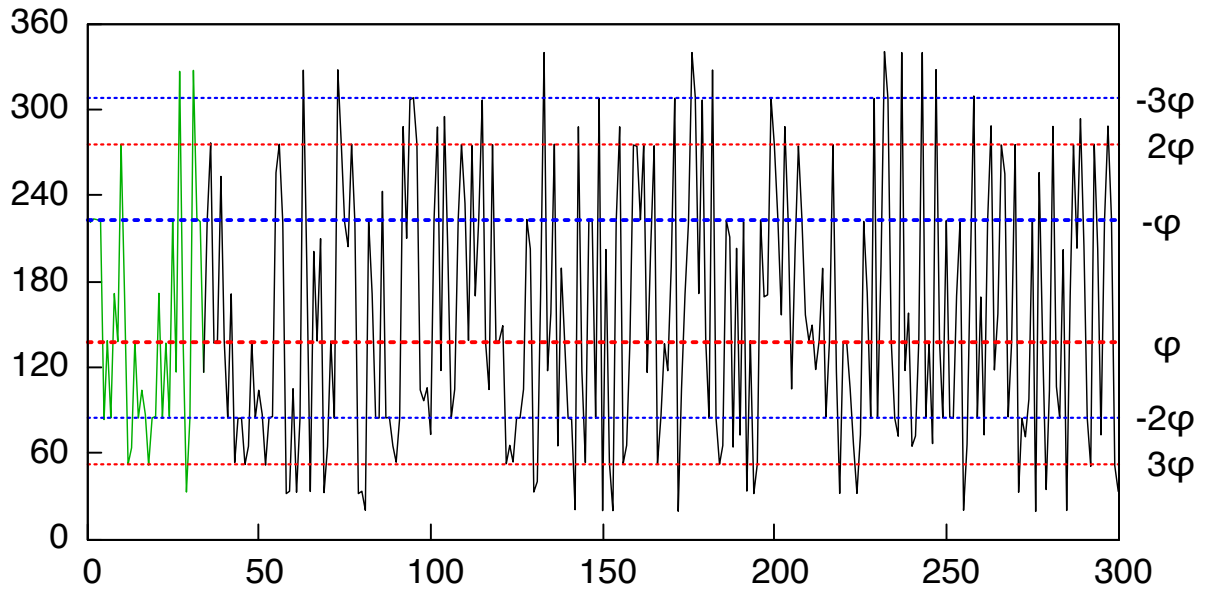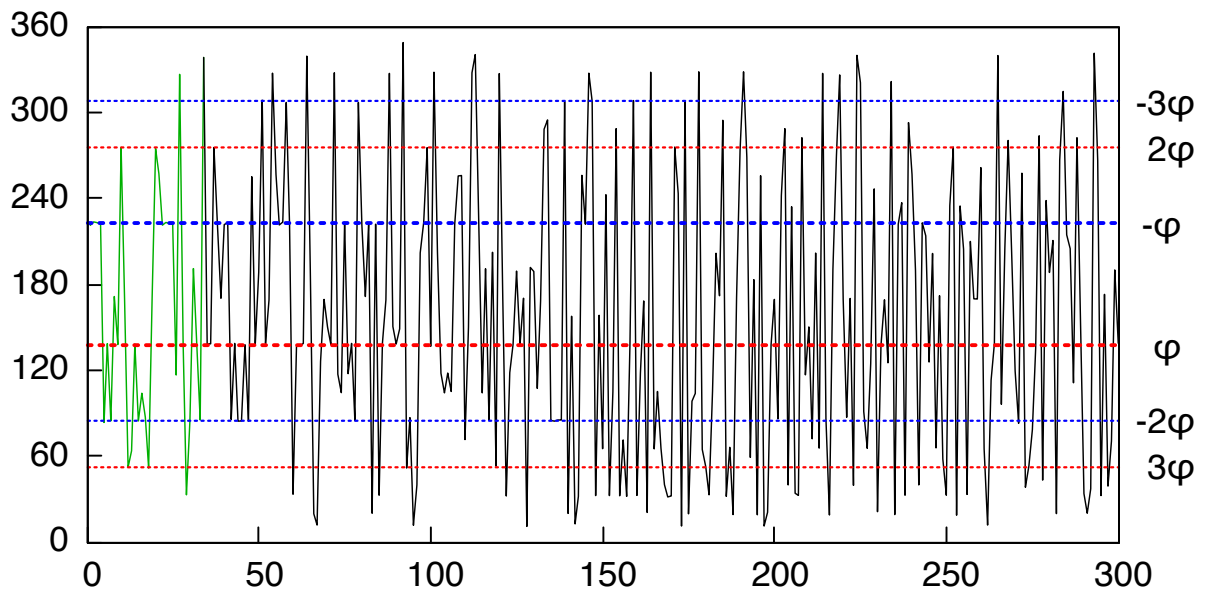
**T Zhang, M Cieslak, A Owens, F Wang, SK Broholm, TH Teeri, P Elomaa, and P Prusinkiewicz**

**Fig. S11.** Divergence angles between the first 300 primordia generated by the gerbera model. (A) The active ring is circular (Fig. 9 C). (B) The active ring is transiently elliptic (Fig. 9 E). Dotted lines indicate the golden angle $\varphi \cong 137.5°$ and its multiples (within the range $0$ to $360°$), which highlights that the differences in the divergence angles are due to the random order of primordia emergence. In spite of these differences, the final phyllotactic pattern is the same.

**T Zhang, M Cieslak, A Owens, F Wang, SK Broholm, TH Teeri, P Elomaa, and P Prusinkiewicz**

Movie S1. (corresponding to Fig. 4I). Simulation of early bract patterning (up to 34 primordia). The simulation is effected using Model 1 (the expanding ring model), overlaid on the composite images of heads showing auxin distribution (DR5 signal) in the corresponding developmental stages. Pauses highlight the simulation stages that correspond most closely to the microscopic images.

Movie S2. (corresponding to Fig. 7). Simulation of the patterning of bract and floret primordia on an expanding disk. The simulation is effected using Model 2 (the disk model), overlaid on the composite images of heads up to the 34-primordium stage. The decreasing radius of the circles that represent primordia reflects the decreasing threshold distance for the insertion of new primordia according to the Hofmeister / Snow & Snow rule. The model captures the differences in the radial position of primordia that become visible at the 21-primordium stage and are pronounced at the 34-primordium stage, as highlighted by the simulation pause. The continuing simulation captures the emergence of parastichies based on the template of bracts and the patterning of florets, which stops when the entire receptacle surface is consumed.

Movie S3. (corresponding to Figs. 8 A and B, and S9). Construction of the data-driven growing receptacle model. The white contour propagating in the top left panel represents changes in the receptacle shape and size over time. This dynamic is captured by computing weighted averages of digitized longitudinal sections of real heads, with the weights changing over time as indicated by the white bar sweeping the plots of individual weight functions in the bottom panel. The top right panel shows the growing receptacle, obtained by revolving the contour around a vertical axis of symmetry. Colors indicate zones that are not occupied by primordia (green), are occupied by bract primordia (yellow) or are occupied by floret primordia (white).

Movie S4. (corresponding to Fig. 8C). Simulation of phyllotactic patterning in gerbera heads on a growing receptacle — side view.

Movie S5. (corresponding to Fig. 9C). Simulation of phyllotactic patterning in gerbera heads on a growing receptacle — top view.

Movie S6. (corresponding to Fig. 9E). A variant of phyllotactic patterning in gerbera heads (Movie 5). The active ring becomes transiently elliptic during the patterning of florets. In spite of the loss of circular symmetry leading to the occurrence of some dislocations (local departures from the mathematically ideal spiral phyllotaxis), the final pattern closely resembles that produced with the circular active ring.

Movie S7. (corresponding to Figs. 8D and 9K). Simulation of phyllotactic patterning in a gerbera head with realistically modeled floret primordia.

## References

1. P Prusinkiewicz, A Lindenmayer, *The Algorithmic Beauty of Plants.* (Springer, New York), (1990).
2. R Karwowski, P Prusinkiewicz, Design and implementation of the L+C modeling language. *Notes Theor Comput. Sci* **86**, 134–152 (2003).
3. P Prusinkiewicz, M Cieslak, P Ferraro, J Hanan, Modeling plant development with L-systems in *Mathematical Modelling in Plant Biology*, ed. RJ Morris. (Springer, Cham), pp. 139–169 (2018).
4. R Smith, et al., A plausible model of phyllotaxis. *Proc Natl Acad Sci U S A* **103**, 1633–1638 (2006).
5. G Mosca, et al., Modeling plant tissue growth and cell division in *Mathematical Modelling in Plant Biology*, ed. RJ Morris. (Springer, Cham), pp. 107–138 (2018).
6. R Bartels, J Beatty, B Barsky, *An Introduction to Splines for Use in Computer Graphics and Geometric Modeling.* (Morgan Kauffman, Los Almos), (1987).
7. E Cohen, R Riesenfeld, G Elber, *Geometric Modeling with Splines: An Introduction.* (A. K. Peters, Natick), (2001).
8. PB de Reuille, et al., MorphoGraphX: A platform for quantifying morphogenesis in 4D. *eLife* **4**, e05864 (2015).
9. L Mündermann, Y Erasmus, B Lane, E Coen, P Prusinkiewicz, Quantitative modeling of *Arabidopsis* development. *Plant Physiol* **139**, 960–968 (2005).
10. M Heisler, et al., Patterns of auxin transport and gene expression during primordium development revealed by live imaging of the Arabidopsis inflorescence meristem. *Curr Biol* **15**, 1899–1911 (2005).
11. S Tähtiharju, et al., Evolution and diversification of the *CYC/TB1* gene family in Asteraceae – a comparative study in gerbera (Mutisieae) and sunflower (Heliantheae). *Mol Biol Evol* **29**, 1155–1166 (2011).
12. F Aurenhammer, R Klein, Voronoi diagrams in *Handbook of Computational Geometry*, eds. JR Sack, J Urrutia. (Elsevier, Amsterdam), pp. 201–290 (2000).
13. TKF Da, D Cohen-Steiner, Advancing front surface reconstruction in *CGAL 4.14.1 User & Reference Manual.* (www.cgal.org), (2019).